Beta-cell adaptation unveiled: The role of myokines in insulin-resistant mice

Alexandrine Liboz, Carine Beaupère, Natacha Roblot, Emma Rousseau, Jean-Yves Tinevez, Sandra Guilmeau, Anne-Françoise Burnol, Dalale Gueddouri, Xavier Prieur, Jean-Sébastien Annicotte, et al.

Cell Reports

Report

Beta-cell adaptation unveiled: The role of myokines in insulin-resistant mice

Graphical abstract

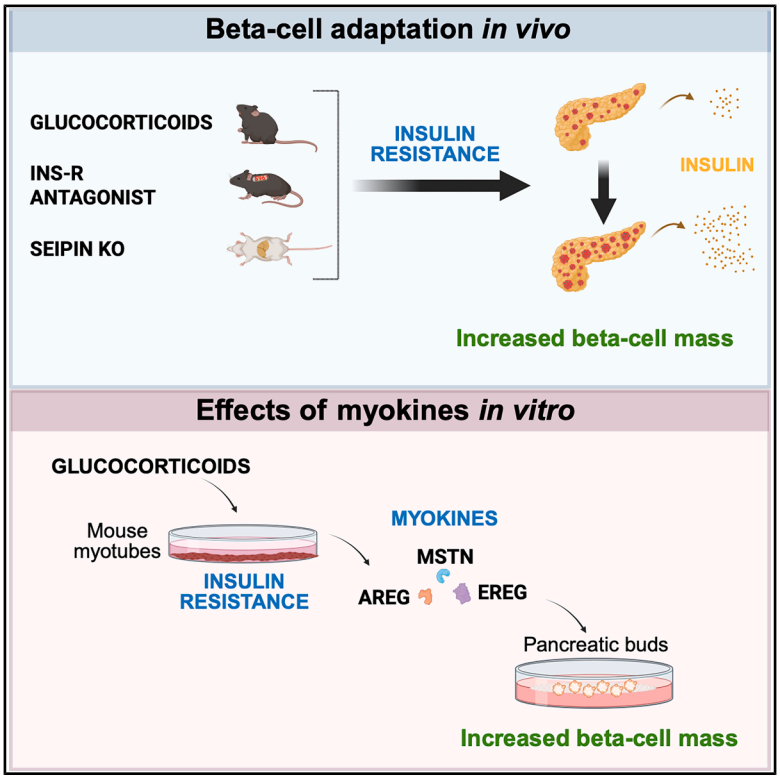

Highlights

- Beta-cell mass increase is shown in several mouse models of insulin resistance
- Whole-pancreas 3D analysis reveals structural adaptation to insulin resistance
- Beta-cell adaptation is maintained with age
- Insulin-resistant muscle cells secrete factors inducing beta-cell differentiation

Authors

Alexandrine Liboz, Carine Beaupère, Natacha Roblot, ..., Bruno Fève, Ghislaine Guillemain, Bertrand Blondeau

Correspondence

bertrand.blondeau@sorbonne-universite.fr

In brief

Pancreatic adaptation through increased beta-cell mass occurs when an increased insulin production is required. Liboz, Beaupere, et al. decipher the mechanisms and signals that regulate such adaptation in mice and identify three myokines inducing beta-cell differentiation *in vitro*.

Liboz et al., 2025, Cell Reports *44*, 116283
September 23, 2025
https://doi.org/10.1016/j.celrep.2025.116283

CellPress

Cell Reports

CellPress
OPEN ACCESS

Report

Beta-cell adaptation unveiled: The role of myokines in insulin-resistant mice

Alexandrine Liboz,[1,2,9] Carine Beaupère,[1,2,9] Natacha Roblot,[1,2] Emma Rousseau,[1,2] Jean-Yves Tinevez,[3] Sandra Guilmeau,[4] Anne-Françoise Burnol,[4] Dalale Gueddouri,[4] Xavier Prieur,[5] Jean-Sébastien Annicotte,[6] Tara L. MacDonald,[7] Bruno Fève,[1,2,8] Ghislaine Guillemain,[1,2,10] and Bertrand Blondeau[1,2,10,11,*]

[1]Sorbonne Université-INSERM, Centre de Recherche Saint-Antoine (CRSA), Paris, France
[2]Institut Hospitalo-Universitaire ICAN, Paris, France
[3]Institut Pasteur, Université Paris Cité, Image Analysis Hub, 75015 Paris, France
[4]Université de Paris, Institut Cochin, CNRS, INSERM, 75014 Paris, France
[5]Nantes Université, CNRS, INSERM, l'Institut du thorax, Nantes, France
[6]University Lille, Inserm, CHU Lille, Institut Pasteur de Lille, U1167 - RID-AGE – Facteurs de risque et déterminants moléculaires des maladies liées au vieillissement, 59000 Lille, France
[7]Department of Physiology, Temerty Faculty of Medicine, University of Toronto, Toronto, ON, Canada
[8]Assistance Publique des Hôpitaux de Paris, Hôpital Saint-Antoine, Service Endocrinologie, CRMR PRISIS, Paris, France
[9]These authors contributed equally
[10]These authors contributed equally
[11]Lead contact
*Correspondence: bertrand.blondeau@sorbonne-universite.fr
https://doi.org/10.1016/j.celrep.2025.116283

SUMMARY

Pancreatic beta cells can adapt their mass and function to maintain normal glycemia when facing peripheral insulin resistance. To clarify the specific contribution and mechanisms of beta-cell mass adaptation in response to insulin resistance, we took advantage of genetic and pharmacologically induced insulin resistance in mice. We uncovered beta-cell expansion, via an increase in pancreatic islet density, as an adaptive mechanism triggered by mild-to-severe insulin resistance in young and older mice and documented pancreatic adaptation using 3D whole-pancreas analysis. Next, we found that insulin-resistant myotubes secrete factors that induce beta-cell differentiation. Using a combination of transcriptomic and functional analysis on a pancreatic differentiation model, we identified that myostatin, amphiregulin, and epiregulin can induce beta-cell differentiation *in vitro*. This work highlights how a physiological adaptation to insulin resistance can unlock the regenerative potential of myotube-derived peptides to trigger adaptive pancreatic beta-cell mass increase.

INTRODUCTION

Beta-cell loss and/or dysfunction are central to the development of diabetes characterized by a deficiency in insulin secretion caused by the dramatic loss of beta-cell mass in both type 1 and type 2 diabetes.[1] During hyperglycemia and/or insulin resistance, beta cells are able to increase their mass as an adaptation to the increased demand for insulin to maintain glucose homeostasis.[2] Research strategies aimed at compensating for beta-cell loss in diabetes have been dampened by our limited understanding of the mechanisms underlying the regulation of pancreatic beta cells in the adult pancreas and its inducing signals, notably in response to insulin resistance.

Stimulating pancreatic beta-cell mass adaptation represents a promising therapeutic avenue to treat insulin deficiency. Yet, the modulation of beta-cell mass in response to insulin resistance—in comparison with other means of pancreatic adaptation i.e., increases in beta-cell function—remains to be defined. To gain robust insights into beta-cell mass adaptation *in vivo*, the use of animal models to study insulin resistance in complementary physiological, genetic, or drug-induced approaches is required.

We previously developed in mice a model of glucocorticoids (GCs)-induced insulin resistance using chronic corticosterone (CORT) treatment and subsequently characterized beta-cell adaptation.[3] GCs are known to alter glucose homeostasis by inhibiting insulin secretion[4]; reducing insulin sensitivity at the liver, muscle, and adipose tissue; and by modulating insulin resistance.[4–7] We showed a massive increase in beta-cell mass driven by islet growth and an increase in islet number. We noted that the increased beta-cell mass was associated with an increase in *Ngn3* expression along with other genes known to be involved in beta-cell differentiation. Strikingly, partial beta-cell mass regeneration after GC treatment occurred even after near-total depletion, suggesting beta-cell regeneration. Finally, we demonstrated that beta-cell mass adaptation was not a direct effect of GCs, but rather regulated by unknown factors in the serum of GC-treated mice.[3] Our model raised the possibility of a substantial increase in beta-cell mass in the pancreas of young-adult mice driven by circulating factors.

Other situations of insulin resistance have been described, but beta-cell adaptation has been partially explored. Hence, mutations in the *BSCL2* gene—encoding seipin, a protein required in lipid droplet formation and maintenance within adipocytes—induces a near-complete loss of adipose tissue, severe insulin resistance, and ultimately diabetes. Mouse model of *Bscl2* gene deletion leads to similar metabolic phenotypes,[8] and adipocyte-specific deletion of *Bscl2* results in progressive lipodystrophy associated with glucose intolerance and insulin resistance.[9] Pancreatic beta-cell function has been assessed in the constitutive model of heterozygous *Bscl2* deletion,[10] but morphological and adaptive mechanisms are unknown. S961, an insulin receptor antagonist causes insulin resistance, hyperinsulinemia, and hyperglycemia.[11] S961 induces beta-cell proliferation in both rats and mice,[12,13] but effects on other aspects of beta-cell mass adaptation remain to be characterized.

The aim of our present study was to (1) better characterize pancreatic adaptation in response to GC-induced insulin resistance compared with other well-described models of insulin resistance, namely the adipocyte-specific deletion of *Bscl2* and S961 models; (2) identify the circulating factors responsible for beta-cell mass adaptation in response to CORT; and (3) identify the signaling pathways involved.[3]

Using multiple mouse models, here we show that (1) mild-to-severe insulin resistance induces beta-cell mass adaptation in young and older mice, (2) there is a threshold of GC exposure and insulin resistance that are necessary to trigger adaptations in beta-cell mass and function, and (3) islet volume and density can be precisely quantified by optimizing 3D analysis of cleared adult mice pancreas. Finally, we analyzed elements of tissue communication between skeletal muscle cells and the pancreas and identified 3 myokines: Myostatin (MSTN, transforming growth factor β [TGF-β] superfamily), Amphiregulin (AREG, epidermal growth factor [EGF] family), and Epiregulin (EREG, EGF family) that trigger beta-cell differentiation *ex vivo*. Interestingly, changes in EGF and VEGF signaling *ex vivo* were also reflected in the pancreatic ducts and islets of CORT-treated animals *in vivo*. All together, our findings suggest that targeting beta-cell mass adaptation could be envisioned as a regenerative therapy in future treatments for diabetes.

RESULTS

Mild-to-severe insulin resistance in young mice predicts beta-cell functional adaptations versus both function and mass adaptations

We previously demonstrated that pancreatic adaptation, with increased beta-cell mass and islet density, occurs in response to 100 μg/mL CORT (C100)-induced insulin resistance in young-adult mice.[3] We next aimed to determine the dynamic relationship between insulin resistance and pancreatic adaptation by challenging mice with lower CORT doses, 25 (C25) or 50 (C50) μg/mL of CORT. After 4 weeks of treatment, insulin tolerance test (ITT) showed a severe insulin resistance in C100- and C50-treated mice and intermediate insulin resistance in the C25 group (Figure 1A). Compared to VEH-treated mice, slopes of early insulin sensitivity were reduced in mice treated with C25, C50, and more severely with C100 (Figure 1B). Fasting plasma insulin levels were respectively increased 17- and 15-fold in C50 and C100 treatments, in comparison to VEH (Figure 1C).

Beta-cell fraction and mass were increased in C50- and C100- but not in C25-treated mice (Figures 1H, 1I, and S1A). Increased beta-cell mass in C50 and C100 was achieved through an increase in mean islet size and islet density (Figures 1J and 1K). Further, *Mki67* expression, a marker of proliferation, was increased in C50 and C100 conditions (Figure 1L). We also noticed a significant increase in the mRNA levels of several genes crucial for function (*Ins1*, *Ins2*, *Abcc8*, *Gck*, *Kcnj11*; Figure 1M) and maturation/identity (*Pdx1*, *Ngn3*, *Rfx6*, *Isl1*, *Nkx2-2/6-1*; Figure 1N) of beta cells in C100 mice.

Taken together, these results demonstrate that mild insulin resistance induced by C25 treatment could lead to beta-cell adaptation solely by a functional increased insulin secretion with no change in beta-cell mass, while more severe insulin resistance (C50–C100) induces both functional and beta-cell mass increases through an increase in beta-cell mass and islet density.

Aging is a limiting process in adaptive mechanisms.[14] Hence, we sought to determine whether the capacity for beta-cell adaptation is maintained in 12-month-old mice in response to moderate and severe CORT-induced insulin resistance. As in young mice, we observed an increase in insulin resistance and serum insulin levels with increasing CORT dose, suggesting the persistence of pancreatic adaptation with age (Figures S1B–S1D). Interestingly, in older mice, C25 treatment resulted in an increase in beta-cell fraction and mass (Figures S1E, S1F, and S1I–S1L), while islet density solely increased in C50 and C100 treatments (Figure S1K). Overall, these results show that the adaptation of beta-cell mass can be induced and maintained in older mice in response to severe insulin resistance.

Further, we explored whether this adaptive mechanism persists in other models of insulin resistance: mice with adipose tissue-specific genetic deletion of *Bscl* (Adipo Seipin knockout [KO]) displayed mild insulin resistance (Figures S2A and S2B), while mice treated with the insulin receptor antagonist S961 show a rapid and severe insulin resistance associated with hyperglycemia[15] compared to controls. Beta-cell fraction was increased (Figures S2C and S2D) with no change in beta-cell mass (Figure S2E) or mean islet size (Figure S2F) but an augmented islet density (Figure S2G) in Adipo Seipin KO, while pancreatic weight and alpha-cell mass and fraction show minimal or no changes (Figures S2H–S2J). Beta-cell fraction was doubled and beta-cell mass increased in S961-treated mice (Figures S2K–S2M). Mean islet size remained unchanged (Figure S2N) but islet density was increased by 50% (Figure S2O), while pancreatic weight and alpha-cell mass were slightly decreased (Figures S2P–S2R). Overall, these results demonstrate that mild-to-severe insulin resistance associates with beta-cell mass and islet density adaptations.

3D analysis of pancreas from CORT-induced insulin-resistant mice confirms increased islet number as an adaptive mechanism to increase beta-cell mass in young adult mice

Generally, the study of pancreatic adaptation relies on morphometric techniques limited to 2D analysis of pancreatic sections[3] or 3D analysis that is restricted to specific areas of the

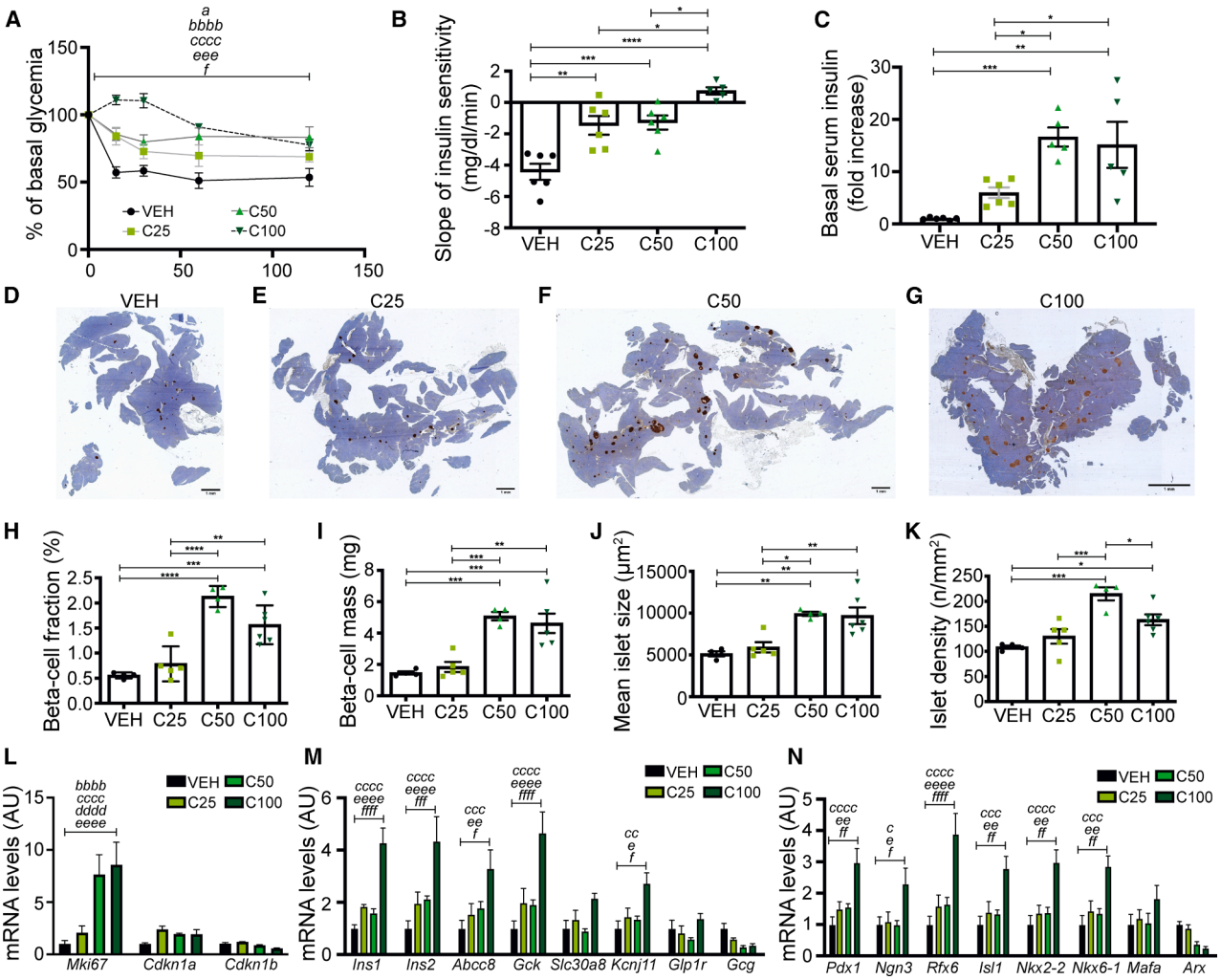

Figure 1. The severity of insulin resistance balances beta-cell functional adaptation vs. function and mass adaptation in young mice

(A and B) (A) Insulin tolerance test, presented as the percentage of basal glycemia, was carried out on mice treated with VEH (n = 6), C25 (n = 6), C50 (n = 6), and C100 (n = 5) for 4 weeks and (B) slopes of early insulin sensitivity between T15 and T0.

(C) Fasted insulin serum levels in mice treated with VEH (n = 6), C25 (n = 6), C50 (n = 5), and C100 (n = 5).

(D–G) Representative images of insulin immunostaining (brown) on hematoxylin (blue) counterstained pancreatic sections of (D) VEH-, (E) C25-, (F) C50-, and (G) C100-treated mice.

(H–K) Pancreatic beta-cell fraction, beta-cell mass, mean islet size, and islet density after insulin immunostaining VEH (n = 4), C25 (n = 5), C50 (n = 4), and C100 (n = 5) mice.

Values are expressed as the mean ± SEM. *p < 0.05; **p < 0.01; ***p < 0.001; ****p < 0.0001 when comparing CORT-treated vs. VEH-treated mice.

(L–N) mRNA levels of (L) cellular cycle, (M) beta-cell function, and (N) beta-cell maturation/identity maintenance genes were determined by quantitative reverse-transcription PCR (RT-qPCR) on isolated islets from (n = 6) VEH-, (n = 5) C25-, (n = 5) C50-, and (n = 4) C100-treated mice.

Values are expressed as the mean ± SEM. [a]C25 vs. VEH; [b]C50 vs. VEH; [c]C100 vs. VEH; [d]C25 vs. C50; [e]C25 vs. C100; and [f]C50 vs. C100; and [x]p < 0.05; [xx]p < 0.01; [xxx]p < 0.001; [xxxx]p < 0.0001.

pancreas.[13,16] Biases from tissue sectioning, histological methods, and sampling (Figure S1A) often preclude an accurate quantification of pancreatic islets necessary to fully characterize beta-cell mass adaptation. These limitations impose a technical gap in our estimation of pancreatic adaptation. To address this, we optimized a 3D model allowing insulin staining and tissue clearing of the whole pancreas (Figure 2A). Our protocol (Figure 2A) allowed for beta-cell detection and tissue clearing to assess whole pancreas volume, whole insulin-immunofluorescence volume, islet counting, and classification of individual volumes of insulin-positive cell clusters. We observed a specific and homogenous staining of insulin-positive cells, regrouped in well-defined circular objects, classified as pancreatic islets (Figures 2B and 2C). Following islets segmentation, 3D reconstructions showed a regular distribution of islets throughout the pancreas, validating our pipeline for image segmentation (Figures 2B and 2C). Whole pancreatic volume was identical in young VEH- and C50-treated mice (Figure 2D) while whole

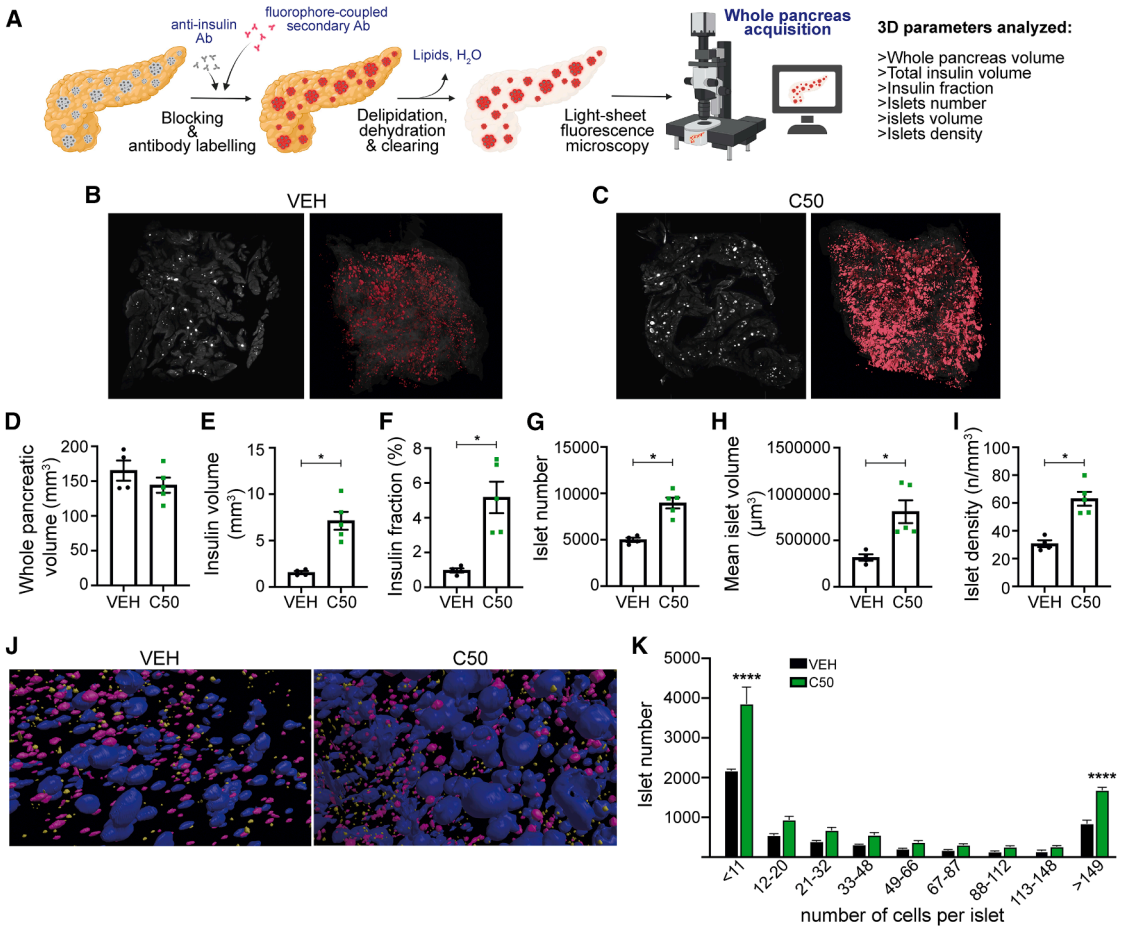

Figure 2. 3D analysis of pancreas from CORT-induced insulin-resistant mice confirms increased islet numbers as an adaptive mechanism in young-adult mice

(A) Schematic representation of the three-dimensional analysis protocol.

(B and C) Representative images of a z stack section after acquisition on whole pancreas stained for insulin using light-sheet microscopy from VEH and C50 mice (left) and representative images of the 3D reconstruction following image segmentation of volume (glass-like structure) and islets (red structures) on whole pancreas from VEH and C50 mice (right).

(D–I) Whole pancreas volume, total insulin volume, insulin fraction, islet number, mean islet volume, and islet density calculated after image segmentation and analysis of pancreas from VEH (n = 4) and C50 (n = 5) mice.

(J) Illustration of islet size diversity and density inside a pancreas of VEH (left) and C50 mouse (right). Islets < 11 cells are represented in yellow; islets 12–148 cells are in pink; islets > 149 cells are in blue.

(K) Islet size distribution in pancreas from VEH (n = 4) and C50 (n = 5) mice. Size categories were defined as indicated in the STAR Methods.

Values are expressed as the mean ± SEM. *p < 0.05, ****p < 0.0001 when comparing CORT-treated vs. VEH-treated mice.

insulin volume was 4.6-fold higher and insulin fraction 5.4-fold higher in C50 mice versus VEH (Figures 2E and 2F). We measured an 80% increased islet number upon C50 challenge (Figure 2G; Video S1) and a 2.6-fold higher mean islet volume in C50 mice (Figure 2H). Comparing the number of islets to the whole pancreatic volume, we demonstrated a 2-fold increase in islet density (Figure 2I). Islet classification revealed a near doubling of both the smallest and the largest classes of cell clusters (Figures 2J and 2K; Video S2) and a trend toward higher islet number in every other class (Figure 2K). Similar trends were found in older mice (Figure S3), albeit to a lesser extent, along with an increase in both small and big classes of cell clusters (Figure S3H).

Taken together, these results unequivocally show increased beta-cell mass and fraction in CORT-treated mice, as well as a doubled islet density and a clear and specific rise in small islet numbers, reflecting increase of islet density as an adaptive process to insulin resistance in mice.

Conditioned medium from CORT-treated myotubes enhances beta-cell differentiation in an *ex vivo* pancreatic bud model

We previously demonstrated that beta-cell mass adaptation in response to CORT was due to the presence of circulating pro-adaptive factors in the serum of mice with GC-induced insulin resistance.[3] We hypothesized that insulin-sensitive organs may

CellPress
OPEN ACCESS

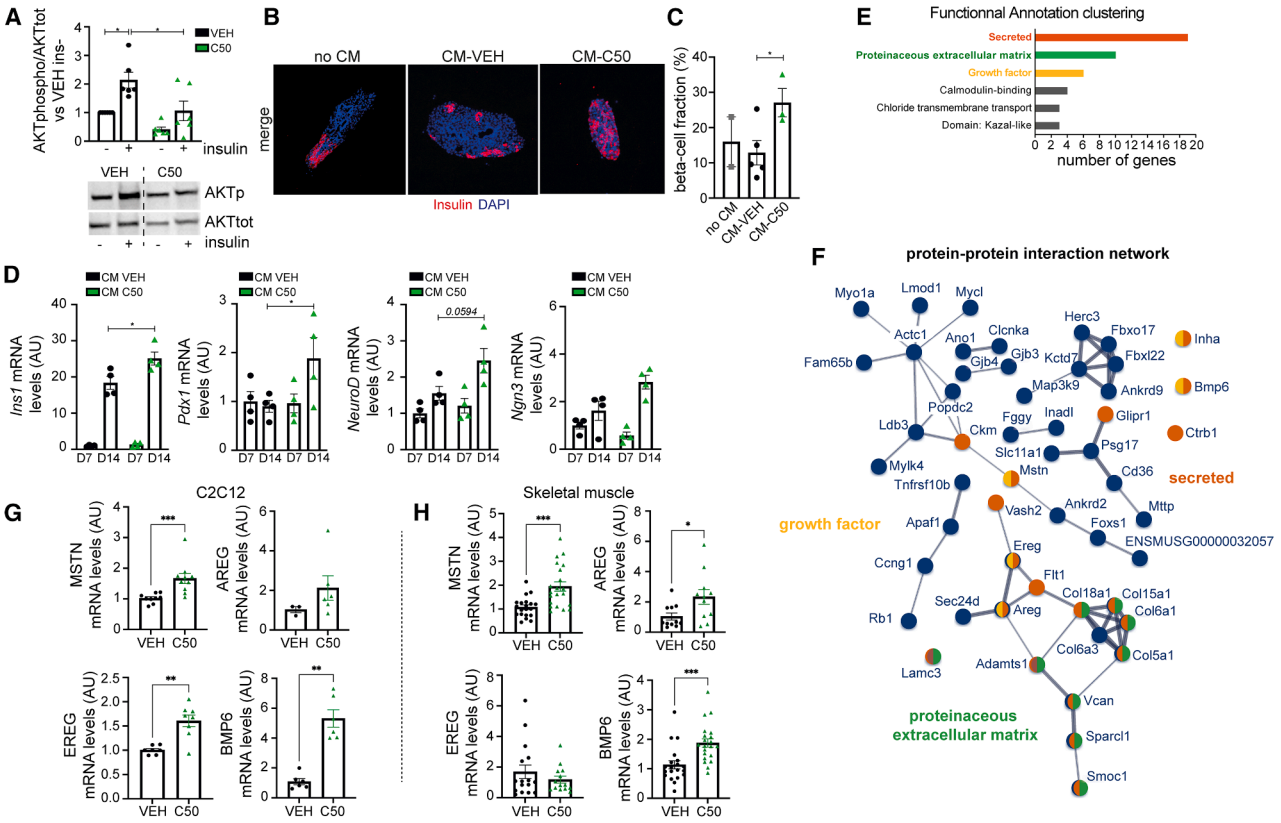

Figure 3. CORT treatment in myotubes induces the expression of genes coding for secreted proteins and growth factors

(A) Resistance to insulin (100 nM) was monitored with the quantification by western blot of the phosphorylated AKT to total-AKT protein ratios in C2C12 differentiated myotubes treated or not with C50 for 24 h. $n = 6$ per condition.

(B and C) Insulin labeling (B) and morphometric quantification (C) were performed on sections of pancreatic bud E11.5 treated for 7 days with the conditioned medium (CM) from CORT ($n = 3$)- or VEH (ethanol, $n = 5$)-treated myotubes followed by 7 days with the treated medium. Untreated pancreatic buds (no CM, $n = 2$) were added for comparison purposes over the direct effect of C2C12 CM.

(D) mRNA levels of the beta-cell maturation/identity maintenance genes *Ins1*, *Pdx1*, *NeuroD*, and *Ngn3* were determined by RT-qPCR on pancreatic buds E11.5 treated for 7 days with CM from VEH- or C50-treated myotubes ±7 days without CM (D14) ($n = 4$ per condition).

(E and F) RNA-seq analysis of myotubes treated for 24 h with either C50 or VEH ($n = 3$ per condition). (E) Adjusted p value (FDR) < 0.1 was used for cutoff, representing a total of 119 differentially expressed genes (DEGs) that were further used for functional annotation clustering using DAVID database. (F) A protein-protein interaction network generated on STRING database using the significantly up-regulated DEGs highlights different functional clusters of genes coding for secreted proteins (orange), components of the extracellular matrix (green), and growth factors (yellow).

(G) *Mstn* (VEH, $n = 9$; C50, $n = 10$), *Areg* (VEH, $n = 3$; C50, $n = 6$), *Ereg* (VEH, $n = 7$; C50, $n = 8$), and *Bmp6* (VEH, $n = 6$; C50, $n = 6$) gene expression validated using RT-qPCR in C2C12 myotubes treated for 24 h with either C50 or VEH (ethanol).

(H) *Mstn* (VEH, $n = 20$; C50, $n = 21$), *Areg* (VEH, n = 11; C50, $n = 10$), *Ereg* (VEH, $n = 16$; C50, $n = 14$), and *Bmp6* (VEH, $n = 20$; C50, $n = 21$) gene expression in skeletal muscle from mice treated for 4 weeks with either VEH (ethanol) or C50 in drinking water. Values are expressed as the mean ± SEM. *$p < 0.05$; **$p < 0.01$; ***$p < 0.001$ when comparing C50-treated vs. VEH-treated C2C12 myotubes, skeletal muscles, or CM-C50 vs. CM-VEH treated pancreatic buds.

produce such factors. Skeletal muscle, the largest insulin sensitive organ in the body, is known to have paracrine and endocrine functions via the release of myokines, metabolites, and exosomes and impact beta-cell survival and proliferation.[5,17,18]

To mimic skeletal muscle to pancreas communication *in vitro*, we treated mouse pancreatic buds with conditioned media collected from C50-treated C2C12 myotubes. We first validated that a 24-h CORT treatment induced insulin resistance, as illustrated by the dampened pAKT/AKT ratio in C50 vs. VEH myotubes following an insulin challenge (Figure 3A). We applied the conditioned medium (CM) from C50 or control myotubes directly to pancreatic buds E11.5 for 7 days (D7) and in CM-free culture for an extra 7 days (D14) to alleviate any direct effect of CORT, as described previously.[3] We observed a significant increase in the beta-cell fraction of CM-C50-treated pancreatic buds shown by insulin labeling (Figures 3B and 3C) at D14 and increased *Ins1* and *Pdx1* expression (Figure 3D). All together, our data indicate that insulin-resistant myotubes secrete factors that can enhance beta-cell differentiation.

CORT treatment in myotubes induces the expression of genes coding for secreted proteins and growth factors

To discover the potential pro-adaptive factors, we used RNA sequencing to analyze the transcriptomic signature of the C50-treated myotubes whose CM was used to treat pancreatic buds. Three biological replicates with 29–35 million reads per replicate

were generated for C50- or VEH-treated myotubes. The high sequencing quality score (Table S1) and consistency in fragments per kilobase million (FPKM) distribution among samples confirmed the low technical variability across samples (Figure S4A). However, principal component analysis did not demonstrate a specific clustering of the two treatment groups, possibly due to the low number of differentially expressed genes (DEGs = 119) in C50- versus VEH-myotubes (false discovery rate [FDR] < 0.1 with 0.5 < log2FC < −0.5; Figures S4B–S4D; Table S2). Interestingly, 101 of the DEGs were up-regulated in C50 (Figure S4D). To identify signatures specific to CORT treatment, we performed gene ontology and functional enrichment analysis using the DAVID and STRING databases (Figures 3E and 3F). The transcriptome of C50-myotubes was enriched for genes coding for secreted proteins (19 genes), growth factors (6 genes), and components of the extracellular matrix (10 genes) (Figure 3E), suggesting that CORT induces a secretory phenotype in myotubes. In order to narrow our list of potential candidates, we decided to exclude genes coding for proteins in the extracellular matrix (Figure 3F). We generated a shortlist of 8 potential candidates whose expression was up-regulated in the C50 dataset (*Areg*, *Ereg*, *Vash2*, *Mstn*, *Ctrb1*, *Bmp6*, *Inha*, and *R3hdml*) (Figure 3E) and evaluated their expression profile at 24 h (Figure 3G) or up to 72 h (Figure S4E) in C50- or VEH-treated myotubes and in skeletal muscle (soleus and gastrocnemius combined) of C50- or VEH-treated mice (Figure 3H). Only 2 genes, *Mstn* and *Bmp6* were overexpressed in response to CORT in both myotubes and skeletal muscle tissues (Figures 3G and 3H), while *Areg* and *Ereg* were up-regulated only in mouse skeletal muscle or in myotubes, respectively (Figures 3G and 3H).

Finally, to identify signaling pathways triggered by CORT, we performed kinome profiling in C50 or VEH pancreatic ducts (Figures S5A–S5E) or islets (Figures S5F–S5J) to characterize serine/threonine or tyrosine kinases whose activity was changed by CORT. Multiple peptides were found to be differentially phosphorylated in the C50 duct protein extract (Figures S5A and S5B), resulting from a change in the activity of several kinases (Figures S5C–S5E). Hence, three main signaling pathways changed in response to CORT: VEGF, EGF, and neurotrophin signaling. Moreover, protein-protein interaction network analysis using STRING-db revealed that AREG and EREG, but not MSTN nor BMP6, are closely related to VEGF, EGF, and neurotrophin (Figure S5E). ERBB4, whose phosphorylation is reduced in CORT-treated pancreatic ducts, is a known receptor of both AREG and EREG.[19] Interestingly, ErbB and VEGF signaling were also changed in pancreatic islets in response to CORT (Figure S5J). Although more experiments are needed to functionally validate the participation of these signaling pathways in beta-cell mass adaptation, these results suggest that circulating AREG and EREG, and more generally EGF ligands, are candidates that may stimulate beta-cell mass adaptation.

MSTN, AREG, and EREG enhance beta-cell differentiation in an *ex vivo* mouse pancreatic bud model

Next, we evaluated whether recombinant proteins AREG, EREG, but also BMP6 and MSTN could directly impact beta-cell differentiation in pancreatic buds at E11.5 (Figure 4). Based on the literature[20–23] and a setup experiment where we titrated protein concentrations (Figures S6A–S6H), we treated pancreatic buds with BMP6 (20 ng/mL), MSTN (100 ng/mL), AREG (500 ng/mL), and EREG (100 ng/mL) for either 3 (D3) or 7 (D7) consecutive days or 14 days with a washout period of 7 days (D14), to mirror experimental conditions in Figure 3. At D7 and D14, the beta-cell and alpha-cell fraction increased in pancreatic buds treated with MSTN, AREG, or EREG (Figures 4A–4C) with no effect of BMP6 (Figures 4A–4C). Expression of beta-cell marker *Ins1*, alpha-cell marker *Gcg*, and delta-cell marker *Sst* were drastically increased from D3 to D14 in MSTN-treated buds. MSTN enhanced the expression of the pro-endocrine master regulator *Ngn3* and downstream targets (*NeuroD* and *Insm1*) along with other pro-endocrine regulators (*Nkx2.2* and *MafA)* at D7 and/or D14 (Figures 4E–4G and S6I–S6R). EREG treatment significantly increased the expression of *Ngn3*, *NeuroD*, *Insm1*, *Nkx2.2*, *Snail, MafA*, and *Arx* from D7 along with the maturation markers *Ins1*, *Gcg*, and *Sst* from D14 (Figures 4 and S6I–S6R). At D7, AREG also induced the expression of *Insm1* (Figure 4G). AREG-treated buds maintained a higher proliferation rate before committing to the endocrine cell lineage, as shown by the induction of the proliferation markers (*Ki67* and *PCNA*) and the expression of proendocrine PDX1 at the protein level (Figures S6E–S6H). Of note, both AREG and EREG reduced the expression of exocrine-cell markers (*Amy2b* and *Cpa2*), further demonstrating that endocrine over exocrine cellular differentiation is favored by these two myokines (Figures 4J and S6Q).

Overall, our data demonstrate that MSTN and EREG enhance endocrine and beta-cell differentiation from either D3 or D7, while AREG first maintains cellular proliferation, to promote cellular differentiation toward the beta-cell lineage at a later stage. These data support the concept that myotubes influence pancreatic adaptation and beta-cell differentiation during insulin resistance by releasing myokines such as MSTN, EREG, and AREG.

DISCUSSION

Our studies demonstrate that insulin resistance—either pharmacologically or genetically induced—associates with pancreatic adaptation through both a functional increase in insulin secretion and/or a beta-cell mass via islet growth and increased islet density. Importantly, pancreatic adaptation by an increased islet density was a conserved mechanism across mild-to-severe insulin resistance in young and older mice. We optimized the iDisco 3D light sheet immunofluorescence technique and demonstrate that GC-induced insulin resistance is associated with an increase in both islet size and number. Finally, we established that insulin-resistant myotubes can secrete factors, namely MSTN, AREG, and EREG, that drive beta-cell differentiation from embryonic precursor cells.

We used two independent models of insulin resistance, *Bscl2*$^{lox/lox}$ × Adipoq-CreER mice and S961-treated mice, and observed beta-cell adaptation trough increased islet density. Thus, insulin resistance could be the driving force behind beta-cell mass adaptation, irrespective of its origin. We also used different doses of CORT to achieve gradual insulin resistance and showed that beta-cell adaptation was driven solely

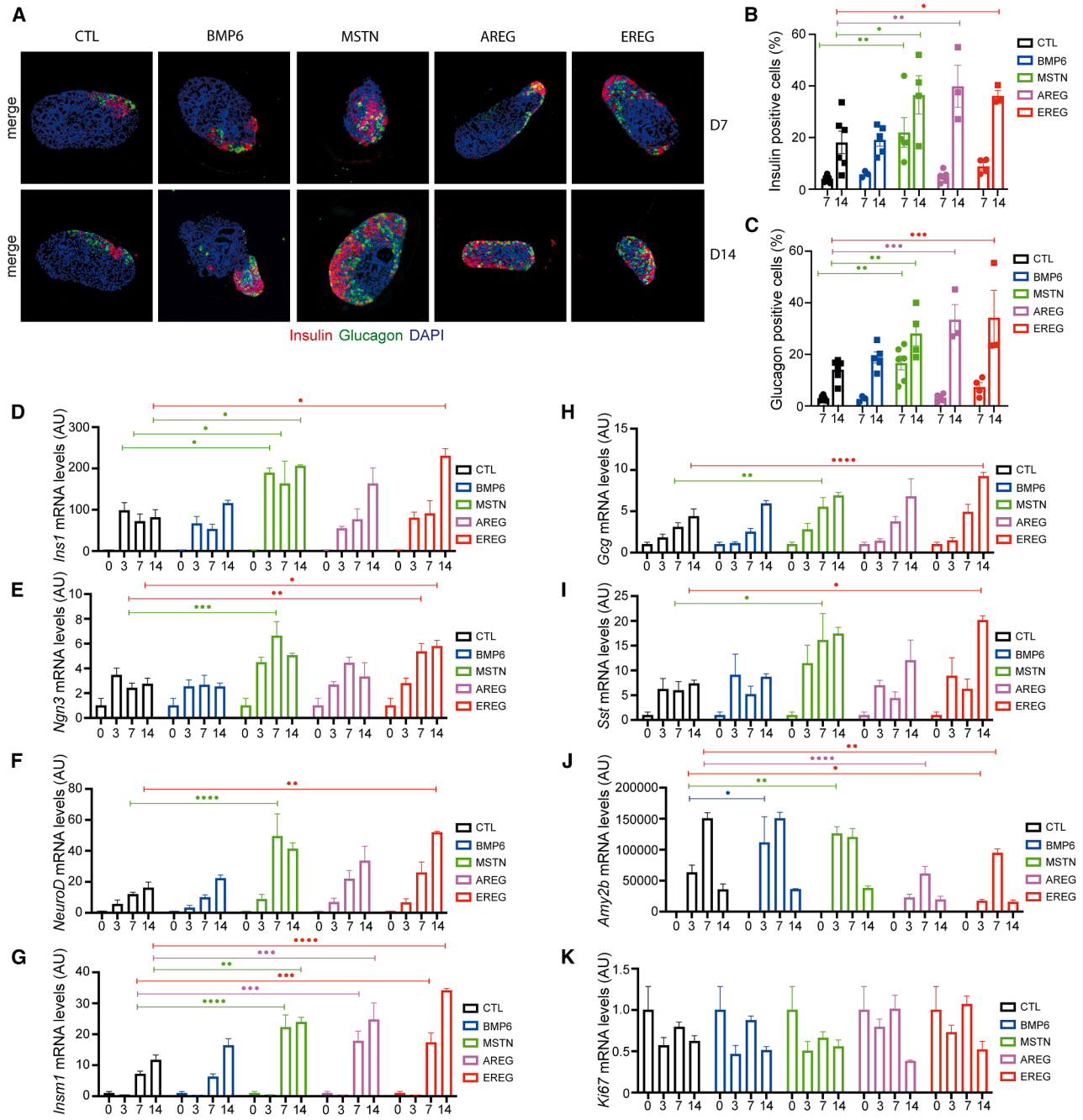

Figure 4. MSTN, AREG, and EREG enhance beta-cell differentiation in an *ex vivo* pancreatic bud model

(A–C) Pancreatic buds E11.5 were treated with recombinant proteins, either BMP6 (20 ng/mL), MSTN (100 ng/mL), AREG (500 ng/mL), or EREG (100 ng/mL) for either 0 (n = 4), 3 (n = 6), 7 (n = 6), or 14 (n = 3) days with a washout period of 7 days. Insulin (A and B) or glucagon (A and C) labeling and subsequential morphometric quantifications (B and C) were performed on pancreatic bud E11.5 tissue sections.

(D–K) Expression of pancreatic pro-endocrine cell maturation/identity maintenance genes (*Ins1*, *Gcg*, *Sst*, *Ngn3*, *NeuroD*, and *Insm1*), exocrine cells (*Amy2b*), and proliferation markers (*Ki67*) were determined by RT-qPCR in pancreatic buds 3, 7, and 14 days post-myokine treatment.

Values are expressed as the mean ± SEM. *p < 0.05; **p < 0.01; ***p < 0.001; ****p < 0.0001 when comparing myokine-treated vs. day 0 pancreatic buds E11.5.

by increasing secretory capacity without stimulating mass adaptation in mild insulin resistance while higher CORT treatment triggered both function and mass adaptation. Aging is associated with insulin resistance in humans and mice, compensated by increased insulin secretion.[24–29] This functional adaptation is concomitant to increased beta-cell mass.[30,31] In our study, older mice exposed to CORT treatment became insulin resistant and were still able to increase beta-cell mass through augmented

islet density, emphasizing the plasticity of pancreatic cells in aged organisms.

We previously demonstrated—using a 2D analysis technique on pancreatic sections—an increase in islet density, notably small.[3] Biases associated with the 2D analysis prompted us to tailored organ clearing for a more detailed morphometric analysis of entire pancreas. Different types of 3D analyses of the pancreas of diet-induced obese mice treated with S961[32] or ob/ob mice[33] showed increases in beta-cell volume and number, suggesting adaptation by beta-cell proliferation in these studies. In our study, a detailed 3D analysis of the endocrine pancreas focused more specifically on islet size classification in response to insulin resistance enabled us to identify small clusters containing as few as 1–3 beta cells. We showed a clear and unbiased increase in beta-cell mass and fraction with a doubled islet number following insulin resistance.

Further, we showed that serum from CORT-treated mice contains factors that induced beta-cell differentiation *in vitro*[3]; we tested the possibility that such factors may originate from skeletal muscle. In this study, we identified myokines—MSTN, AREG, and EREG—as stimulants of beta-cell differentiation *ex vivo*, triggering the expression of key transcription factors essential for beta-cell differentiation and maturation (Ngn3, MafA, Nkx2.2, and Insm1) alongside factors that control proliferation (PCNA and Ki67). AREG and EREG are both members of the EGF family. EREG was shown to induce proliferation and enhance insulin secretion *in vitro* in INS-1E and RINm5F beta-cell lines.[34] MSTN is a member of the TGF-β protein family and acts as a key regulator of muscle mass and development.[35] Our results unveil a direct communication axis that exists between insulin-resistant skeletal muscle and beta-cell precursors, leading to enhanced beta-cell mass *in vitro*, which remains to be confirmed *in vivo*.

Recently, Quadir et al. identified an ALK3 high, PDX1/P2RY1^{+} progenitor cell population enriched in the vicinity of pancreatic ducts and pancreatic duct glands, but not in pancreatic islets,[36,37] able to expand and differentiate toward insulin^{+} cells upon transient treatment with BMP7. Another BMP, BMP6, was identified in our screen and failed to improve beta-cell differentiation in our hands, perhaps due to acute and non-transient treatment.

Our results offer a broad view of beta-cell mass adaptation in several models of genetic or pharmacological insulin resistance. Our study demonstrates that the level of pancreatic adaptation depends on both duration and severity of insulin resistance and that age is not a barrier to pancreatic adaptation by increased islet number. The use of an optimized whole organ 3D analysis allowed us to show a robust increase in beta-cell mass and could be further used as a tool to monitor the efficacy of therapeutic strategies aiming at increasing beta-cell mass. Finally, we identified 3 myokines whose expressions are increased during insulin resistance that can stimulate beta-cell differentiation *in vitro*, representing promising candidates to regenerate a functional beta-cell mass in the pancreas.

Limitations of the study

In several models of insulin resistance, we observed increased islet density and numbers, including through unbiased 3D analysis, that may result from the formation of new beta cells from precursors but without an identifiable source. Moreover, we have shown that myokines stimulate beta-cell differentiation in an *in vitro* model of pancreatic buds from mouse embryos. It is now required to define whether similar effects can be obtained on adult tissues (cultured pancreatic slices for example) and *in vivo* in mice.

RESOURCE AVAILABILITY

Lead contact

Requests for further information and resources should be directed to and will be fulfilled by the lead contact, Bertrand Blondeau (bertrand.blondeau@sorbonne-universite.fr).

Materials availability

For transcriptomic data, raw reads (fastq files) and raw count tables have been deposited on NCBI repository under the accession number NCBI GEO GSE261984. Code and video are available on Mendeley (Mendeley data: https://doi.org/10.17632/3c954wd6k6.1). All other materials or information are available upon request.

Data and code availability

- Bulk RNA-seq data have been deposited at GEO, and data stored on Mendeley are publicly available as of the publication date. Accession numbers are listed in the key resources table.
- Microscopy data reported in this paper will be shared by the lead contact upon request.
- This paper reports original code available on Mendeley (https://doi.org/10.17632/3c954wd6k6.1).
- Any additional information required to reanalyze the data reported in this work is available from the lead contact upon request.

ACKNOWLEDGMENTS

This work was funded by Inserm, Sorbonne Université, Fondation pour la Recherche Médicale (FRM EQU201903007868 and FRM EQU202103012732), Société Francophone du Diabète, Aide aux Jeunes Diabétiques, Type 1 Running Team, and World Diabetes Tour. We gratefully acknowledge the UtechS Photonic BioImaging (Imagopole), especially Julien Fernandes, C2RT, and Institut Pasteur. We acknowledge the France-BioImaging infrastructure supported by the French National Research Agency (ANR-10-INBS-04). The authors thank T. Ledent, L. Dinard, A. Guyomard, T. Coulais, and Q. Pointout (animal housing facility, Saint-Antoine Research Center, Sorbonne University, INSERM, Paris); R. Morrichon (Cell Imaging and Confocal Microscopy Platform); and Elodie Carotine. A.L. was supported by a doctoral fellowship from Ministère de l'Enseignement Supérieur et de la Recherche and Société Francophone du Diabète.

AUTHOR CONTRIBUTIONS

Conceptualization, B.B. and G.G.; methodology, B.B., G.G., A.L., C.B., and J.-Y.T.; investigation, B.B., G.G., A.L., C.B., N.R., and E.R.; writing—original draft, B.B., G.G., A.L., and C.B.; writing—review & editing, B.B., G.G., A.L., C.B., B.F., S.G., A.-F.B., D.G., J.-Y.T., T.L.M., J.-S.A., and X.P.; funding acquisition, B.B., G.G., C.B., A.L., and B.F.; resources, J.-Y.T., S.G., A.-F.B., D.G., and X.P.; and supervision, B.B. and G.G.

DECLARATION OF INTERESTS

The authors declare no competing interests.

STAR★METHODS

Detailed methods are provided in the online version of this paper and include the following:

SUPPLEMENTAL INFORMATION

Supplemental information can be found online at https://doi.org/10.1016/j.celrep.2025.116283.

Received: April 4, 2024
Revised: July 16, 2025
Accepted: August 22, 2025

REFERENCES

1. Butler, A.E., Janson, J., Soeller, W.C., and Butler, P.C. (2003). Increased beta cell apoptosis prevents adaptive increase in beta cell mass in mouse model of type 2 diabetes: evidence for role of islet amyloid formation rather than direct action of amyloid. Diabetes *52*, 2304–2314. https://doi.org/10.2337/diabetes.52.9.2304.
2. Inaishi, J., and Saisho, Y. (2020). Beta cell Mass in Obesity and Type 2 Diabetes, and Its Relation to Pancreas Fat: A Mini-Review. Nutrients *12*, 3846. https://doi.org/10.3390/nu12123846.
3. Courty, E., Besseiche, A., Do, T.T.H., Liboz, A., Aguid, F.M., Quilichini, E., Buscato, M., Gourdy, P., Gautier, J.F., Riveline, J.P., et al. (2019). Adaptive beta cell Neogenesis in the Adult Mouse in Response to Glucocorticoid-Induced Insulin Resistance. Diabetes *68*, 95–108. https://doi.org/10.2337/db17-1314.
4. Lambillotte, C., Gilon, P., and Henquin, J.C. (1997). Direct glucocorticoid inhibition of insulin secretion. An in vitro study of dexamethasone effects in mouse islets. J. Clin. Investig. *99*, 414–423. https://doi.org/10.1172/JCI119175.
5. Beaupere, C., Liboz, A., Feve, B., Blondeau, B., and Guillemain, G. (2021). Molecular Mechanisms of Glucocorticoid-Induced Insulin Resistance. Int. J. Mol. Sci. *22*, 623. https://doi.org/10.3390/ijms22020623.
6. Fransson, L., Franzen, S., Rosengren, V., Wolbert, P., Sjoholm, A., and Ortsater, H. (2013). beta cell adaptation in a mouse model of glucocorticoid-induced metabolic syndrome. J. Endocrinol. *219*, 231–241. https://doi.org/10.1530/JOE-13-0189.
7. Rafacho, A., Ortsäter, H., Nadal, A., and Quesada, I. (2014). Glucocorticoid treatment and endocrine pancreas function: implications for glucose homeostasis, insulin resistance and diabetes. J. Endocrinol. *223*, R49–R62. https://doi.org/10.1530/JOE-14-0373.
8. Sollier, C., Vatier, C., Capel, E., Lascols, O., Auclair, M., Janmaat, S., Fève, B., Jéru, I., and Vigouroux, C. (2020). Lipodystrophic syndromes: From diagnosis to treatment. Ann. Endocrinol. *81*, 51–60. https://doi.org/10.1016/j.ando.2019.10.003.
9. Combot, Y., Salo, V.T., Chadeuf, G., Hölttä, M., Ven, K., Pulli, I., Ducheix, S., Pecqueur, C., Renoult, O., Lak, B., et al. (2022). Seipin localizes at endoplasmic-reticulum-mitochondria contact sites to control mitochondrial calcium import and metabolism in adipocytes. Cell Rep. *38*, 110213. https://doi.org/10.1016/j.celrep.2021.110213.
10. Xiong, J., Sun, P., Wang, Y., Hua, X., Song, W., Wang, Y., Wu, J., Yu, W., Liu, G., and Chen, L. (2020). Heterozygous deletion of Seipin in islet beta cells of male mice has an impact on insulin synthesis and secretion through reduced PPARgamma expression. Diabetologia *63*, 338–350. https://doi.org/10.1007/s00125-019-05038-x.
11. Vikram, A., and Jena, G. (2010). S961, an insulin receptor antagonist causes hyperinsulinemia, insulin-resistance and depletion of energy stores in rats. Biochem. Biophys. Res. Commun. *398*, 260–265. https://doi.org/10.1016/j.bbrc.2010.06.070.
12. Okamoto, H., Cavino, K., Na, E., Krumm, E., Kim, S.Y., Cheng, X., Murphy, A.J., Yancopoulos, G.D., and Gromada, J. (2017). Glucagon receptor inhibition normalizes blood glucose in severe insulin-resistant mice. Proc. Natl. Acad. Sci. USA *114*, 2753–2758. https://doi.org/10.1073/pnas.1621069114.
13. Tokumoto, S., Yabe, D., Tatsuoka, H., Usui, R., Fauzi, M., Botagarova, A., Goto, H., Herrera, P.L., Ogura, M., and Inagaki, N. (2020). Generation and Characterization of a Novel Mouse Model That Allows Spatiotemporal Quantification of Pancreatic beta cell Proliferation. Diabetes *69*, 2340–2351. https://doi.org/10.2337/db20-0290.
14. Rankin, M.M., and Kushner, J.A. (2009). Adaptive beta cell proliferation is severely restricted with advanced age. Diabetes *58*, 1365–1372. https://doi.org/10.2337/db08-1198.
15. Gueddouri, D., Caüzac, M., Fauveau, V., Benhamed, F., Charifi, W., Beaudoin, L., Rouland, M., Sicherre, F., Lehuen, A., Postic, C., et al. (2022). Insulin resistance per se drives early and reversible dysbiosis-mediated gut barrier impairment and bactericidal dysfunction. Mol. Metab. *57*, 101438. https://doi.org/10.1016/j.molmet.2022.101438.
16. Gribben, C., Lambert, C., Messal, H.A., Hubber, E.L., Rackham, C., Evans, I., Heimberg, H., Jones, P., Sancho, R., and Behrens, A. (2023). Ductal Ngn3-expressing progenitors contribute to adult beta cell neogenesis in the pancreas. Cell Stem Cell *30*, 498–499. https://doi.org/10.1016/j.stem.2023.02.005.
17. Mizgier, M.L., Cataldo, L.R., Gutierrez, J., Santos, J.L., Casas, M., Llanos, P., Contreras-Ferrat, A.E., Moro, C., Bouzakri, K., and Galgani, J.E. (2017). Effect of Human Myotubes-Derived Media on Glucose-Stimulated Insulin Secretion. J. Diabetes Res. *2017*, 1328573. https://doi.org/10.1155/2017/1328573.
18. Zhang, H., Mulya, A., Nieuwoudt, S., Vandanmagsar, B., McDowell, R., Heintz, E.C., Zunica, E.R.M., Collier, J.J., Bozadjieva-Kramer, N., Seeley, R.J., et al. (2023). GDF15 Mediates the Effect of Skeletal Muscle Contraction on Glucose-Stimulated Insulin Secretion. Diabetes *72*, 1070–1082. https://doi.org/10.2337/db22-0019.
19. Lucas, L.M., Dwivedi, V., Senfeld, J.I., Cullum, R.L., Mill, C.P., Piazza, J.T., Bryant, I.N., Cook, L.J., Miller, S.T., Lott, J.H., 4th, et al. (2022). The Yin and Yang of ERBB4: Tumor Suppressor and Oncoprotein. Pharmacol. Rev. *74*, 18–47. https://doi.org/10.1124/pharmrev.121.000381.
20. Traore, M., Noviello, C., Vergnol, A., Gentil, C., Halliez, M., Saillard, L., Gelin, M., Forand, A., Lemaitre, M., Guesmia, Z., et al. (2024). GDF5 as a rejuvenating treatment for age-related neuromuscular failure. Brain *147*, 3834–3848. https://doi.org/10.1093/brain/awae107.
21. von Joest, M., Chen, C., Douché, T., Chantrel, J., Chiche, A., Gianetto, Q. G., Matondo, M., and Li, H. (2022). Amphiregulin mediates non-cell-autonomous effect of senescence on reprogramming. Cell Rep. *40*, 111074. https://doi.org/10.1016/j.celrep.2022.111074.
22. Wang, J.F., Lee, M.S., Tsai, T.L., Leiferman, E.M., Trask, D.J., Squire, M. W., and Li, W.J. (2019). Bone Morphogenetic Protein-6 Attenuates Type 1 Diabetes Mellitus-Associated Bone Loss. Stem Cells Transl. Med. *8*, 522–534. https://doi.org/10.1002/sctm.18-0150.
23. Yasmeen, R., Shen, Q., Lee, A., Leung, J.H., Kowdley, D., DiSilvestro, D.J., Xu, L., Yang, K., Maiseyeu, A., Bal, N.C., et al. (2018). Epiregulin induces leptin secretion and energy expenditure in high-fat diet-fed mice. J. Endocrinol. *239*, 377–388. https://doi.org/10.1530/JOE-18-0289.

24. Aguayo-Mazzucato, C., van Haaren, M., Mruk, M., Lee, T.B., Jr., Crawford, C., Hollister-Lock, J., Sullivan, B.A., Johnson, J.W., Ebrahimi, A., Dreyfuss, J.M., et al. (2017). beta Cell Aging Markers Have Heterogeneous Distribution and Are Induced by Insulin Resistance. Cell Metab. *25*, 898–910.e5. https://doi.org/10.1016/j.cmet.2017.03.015.

25. Arda, H.E., Li, L., Tsai, J., Torre, E.A., Rosli, Y., Peiris, H., Spitale, R.C., Dai, C., Gu, X., Qu, K., et al. (2016). Age-Dependent Pancreatic Gene Regulation Reveals Mechanisms Governing Human beta Cell Function. Cell Metab. *23*, 909–920. https://doi.org/10.1016/j.cmet.2016.04.002.

26. Avrahami, D., Li, C., Zhang, J., Schug, J., Avrahami, R., Rao, S., Stadler, M.B., Burger, L., Schübeler, D., Glaser, B., and Kaestner, K.H. (2015). Aging-Dependent Demethylation of Regulatory Elements Correlates with Chromatin State and Improved beta Cell Function. Cell Metab. *22*, 619–632. https://doi.org/10.1016/j.cmet.2015.07.025.

27. Ehrhardt, N., Cui, J., Dagdeviren, S., Saengnipanthkul, S., Goodridge, H. S., Kim, J.K., Lantier, L., Guo, X., Chen, Y.D.I., Raffel, L.J., et al. (2019). Adiposity-Independent Effects of Aging on Insulin Sensitivity and Clearance in Mice and Humans. Obesity *27*, 434–443. https://doi.org/10.1002/oby.22418.

28. Helman, A., Klochendler, A., Azazmeh, N., Gabai, Y., Horwitz, E., Anzi, S., Swisa, A., Condiotti, R., Granit, R.Z., Nevo, Y., et al. (2016). p16(Ink4a)-induced senescence of pancreatic beta cells enhances insulin secretion. Nat. Med. *22*, 412–420. https://doi.org/10.1038/nm.4054.

29. Tuduri, E., Soriano, S., Almagro, L., Montanya, E., Alonso-Magdalena, P., Nadal, A., and Quesada, I. (2022). The pancreatic beta cell in ageing: Implications in age-related diabetes. Ageing Res. Rev. *80*, 101674. https://doi.org/10.1016/j.arr.2022.101674.

30. Saisho, Y., Butler, A.E., Manesso, E., Elashoff, D., Rizza, R.A., and Butler, P.C. (2013). beta cell mass and turnover in humans: effects of obesity and aging. Diabetes Care *36*, 111–117.

31. Xin, Y., Kim, J., Okamoto, H., Ni, M., Wei, Y., Adler, C., Murphy, A.J., Yancopoulos, G.D., Lin, C., and Gromada, J. (2016). RNA Sequencing of Single Human Islet Cells Reveals Type 2 Diabetes Genes. Cell Metab. *24*, 608–615. https://doi.org/10.1016/j.cmet.2016.08.018.

32. Roostalu, U., Lercke Skytte, J., Gravesen Salinas, C., Klein, T., Vrang, N., Jelsing, J., and Hecksher-Sørensen, J. (2020). 3D quantification of changes in pancreatic islets in mouse models of diabetes type I and II. Dis. Model. Mech. *13*, dmm045351. https://doi.org/10.1242/dmm.045351.

33. Parween, S., Kostromina, E., Nord, C., Eriksson, M., Lindström, P., and Ahlgren, U. (2016). Intra-islet lesions and lobular variations in beta cell mass expansion in ob/ob mice revealed by 3D imaging of intact pancreas. Sci. Rep. *6*, 34885. https://doi.org/10.1038/srep34885.

34. Kuntz, E., Broca, C., Komurasaki, T., Kaltenbacher, M.C., Gross, R., Pinget, M., and Damgé, C. (2005). Effect of epiregulin on pancreatic beta cell growth and insulin secretion. Growth Factors *23*, 285–293. https://doi.org/10.1080/08977190500233367.

35. Camporez, J.P.G., Petersen, M.C., Abudukadier, A., Moreira, G.V., Jurczak, M.J., Friedman, G., Haqq, C.M., Petersen, K.F., and Shulman, G. I. (2016). Anti-myostatin antibody increases muscle mass and strength and improves insulin sensitivity in old mice. Proc. Natl. Acad. Sci. USA *113*, 2212–2217. https://doi.org/10.1073/pnas.1525795113.

36. Qadir, M.M.F., Álvarez-Cubela, S., Klein, D., Lanzoni, G., García-Santana, C., Montalvo, A., Pláceres-Uray, F., Mazza, E.M.C., Ricordi, C., Inverardi, L.A., et al. (2018). P2RY1/ALK3-Expressing Cells within the Adult Human Exocrine Pancreas Are BMP-7 Expandable and Exhibit Progenitor-like Characteristics. Cell Rep. *22*, 2408–2420. https://doi.org/10.1016/j.celrep.2018.02.006.

37. Qadir, M.M.F., Álvarez-Cubela, S., Klein, D., van Dijk, J., Muñiz-Anquela, R., Moreno-Hernández, Y.B., Lanzoni, G., Sadiq, S., Navarro-Rubio, B., García, M.T., et al. (2020). Single-cell resolution analysis of the human pancreatic ductal progenitor cell niche. Proc. Natl. Acad. Sci. USA *117*, 10876–10887. https://doi.org/10.1073/pnas.1918314117.

38. Guillemain, G., Filhoulaud, G., Da Silva-Xavier, G., Rutter, G.A., and Scharfmann, R. (2007). Glucose is necessary for embryonic pancreatic endocrine cell differentiation. J. Biol. Chem. *282*, 15228–15237.

39. Magusto, J., Beaupère, C., Afonso, M.B., Auclair, M., Delaunay, J.L., Soret, P.A., Courtois, G., Aït-Slimane, T., Housset, C., Jéru, I., et al. (2022). The necroptosis-inducing pseudokinase mixed lineage kinase domain-like regulates the adipogenic differentiation of pre-adipocytes. iScience *25*, 105166. https://doi.org/10.1016/j.isci.2022.105166.

40. Kim, D., Paggi, J.M., Park, C., Bennett, C., and Salzberg, S.L. (2019). Graph-based genome alignment and genotyping with HISAT2 and HISAT-genotype. Nat. Biotechnol. *37*, 907–915. https://doi.org/10.1038/s41587-019-0201-4.

41. Anders, S., Pyl, P.T., and Huber, W. (2015). HTSeq–a Python framework to work with high-throughput sequencing data. Bioinformatics *31*, 166–169. https://doi.org/10.1093/bioinformatics/btu638.

42. Dillies, M.A., Rau, A., Aubert, J., Hennequet-Antier, C., Jeanmougin, M., Servant, N., Keime, C., Marot, G., Castel, D., Estelle, J., et al. (2013). A comprehensive evaluation of normalization methods for Illumina high-throughput RNA sequencing data analysis. Brief. Bioinform. *14*, 671–683. https://doi.org/10.1093/bib/bbs046.

43. Szklarczyk, D., Kirsch, R., Koutrouli, M., Nastou, K., Mehryary, F., Hachilif, R., Gable, A.L., Fang, T., Doncheva, N.T., Pyysalo, S., et al. (2023). The STRING database in 2023: protein-protein association networks and functional enrichment analyses for any sequenced genome of interest. Nucleic Acids Res. *51*, D638–D646. https://doi.org/10.1093/nar/gkac1000.

44. Kanehisa, M., and Goto, S. (2000). KEGG: kyoto encyclopedia of genes and genomes. Nucleic Acids Res. *28*, 27–30. https://doi.org/10.1093/nar/28.1.27.

45. Bourouh, C., Courty, E., Rolland, L., Pasquetti, G., Gromada, X., Rabhi, N., Carney, C., Moreno, M., Boutry, R., Caron, E., et al. (2022). The transcription factor E2F1 controls the GLP-1 receptor pathway in pancreatic beta cells. Cell Rep. *40*, 111170. https://doi.org/10.1016/j.celrep.2022.111170.

46. Duquenne, M., Folgueira, C., Bourouh, C., Millet, M., Silva, A., Clasadonte, J., Imbernon, M., Fernandois, D., Martinez-Corral, I., Kusumakshi, S., et al. (2021). Leptin brain entry via a tanycytic LepR-EGFR shuttle controls lipid metabolism and pancreas function. Nat. Metab. *3*, 1071–1090. https://doi.org/10.1038/s42255-021-00432-5.

STAR★METHODS

KEY RESOURCES TABLE

REAGENT or RESOURCE	SOURCE	IDENTIFIER
Antibodies		
monoclonal anti-insulin antibody	Sigma-Aldrich, St. Louis, MO	#I2018 clone K36AC10; RRID AB_260137
monoclonal anti-glucagon antibody	LifeTechnologies	PA5-88091; RRID AB_2804644
Doliclus biflorus agglutinin biotinylated	vectorlab	B1035; RRID AB_2314288
Insulin anti rat antibody	abcam	Ab 181547; RRID AB_2716761
Alexa 750 goat anti mouse antibody	LifeTechnologies	A21037; RRID AB_2535708
Streptavidine-cyanine5	vectorlab	SA1500
Alexa Fluor 488 donkey anti rabbit antibody	LifeTechnologies	A21206; RRID AB_2535792
Alexa Fluor 546 donkey anti mouse antibody	LifeTechnologies	A10036; RRID AB_11180613
Alexa Fluor 546 donkey anti rabbit antibody	LifeTechnologies	A10040; RRID AB_2534016
Alexa fluor goat anti-rat 555 antibody	LifeTechnologies	A21434; RRID AB_141733
Anti AKT antibody	Cell signaling	9272S; RRID AB_329827
Anti-Phospho-akt (ser473) antibody	Cell signaling	9271S; RRID AB_329825
Anti PDX1 antibody		Guillemain et al.[38]
Anti Ki67 antibody	Abcam	Ab15580; RRID AB_443209
Anti PCNA (FL-261) antibody	Santa Cruz Biotechnology	SC-7907; RRID AB_2160375
Anti alpha-Tubulin antibody	Sigma-Aldrich	T5168-2ML, RRID AB_477579
Anti mouse HRP conjugated antibody	Cell Signaling	7076S; RRID AB_330924
Anti Rabbit HRP conjugated antibody	Cell signaling	7074S; RRID AB_2099233
Chemicals, peptides, and recombinant proteins		
Corticosterone	Sigma-Aldrich, St. Louis, MO	27840
S961	Novo Nordisk	NN0069-961
Human insulin ACTAPID PENFILL 100IU/mL	Novo Nordisk	MI-05CFA
Collagenase from clostridium histolyticum	Sigma-Aldrich	C7657
BMP6 recombinant protein, lot TPI0320121	R&D system	6325-BM
MSTN (myostatin) recombinant protein, lot EZG7419091	R&D system	788-G8
AREG (amphiregulin) recombinant protein lot FIF1221042	R&D system	989-AR
EREG (epiregulin) recombinant protein lot FWP0321031	R&D system	1068-EP
Dichloromethane	Sigma-Aldrich, St. Louis, MO	270997-1L
Dibenzyl ether	Sigma-Aldrich, St. Louis, MO	33630-1L
Gelatin	Sigma-Aldrich, St. Louis, MO	48723-500-F
TRITON 100X	Sigma-Aldrich, St. Louis, MO	T8787
Saponin	Sigma-Aldrich, St. Louis, MO	S4521
Critical commercial assays		
insulin immunoassay	Merck, Millipore	EZRMI-13K
RNeasy Mini Plus Kit	QIAGEN, Hilden, Germany	74136
RNeasy Micro Plus Kit	QIAGEN, Hilden, Germany	74004
Deposited data		
C2C12 myotubes treated with corticosterone 10-7M for 24H, rep1, fastq	NCBI GEO	GSM8155523
C2C12 myotubes treated with corticosterone 10-7M for 24H, rep2, fastq	NCBI GEO	GSM8155524
C2C12 myotubes treated with corticosterone 10-7M for 24H, rep3, fastq	NCBI GEO	GSM8155525

(*Continued on next page*)

Continued

REAGENT or RESOURCE	SOURCE	IDENTIFIER
C2C12 myotubes treated with ethanol (1/1000) for 24H, rep1, fastq	NCBI GEO	GSM8155526
C2C12 myotubes treated with ethanol (1/1000) for 24H, rep2, fastq	NCBI GEO	GSM8155527
C2C12 myotubes treated with ethanol (1/1000) for 24H, rep3, fastq	NCBI GEO	GSM8155528
genes.readcount.annot_C2C12.txt, normalized read count	NCBI GEO	GSE261984
Experimental models: Cell lines		
C2C12 mouse myoblast cells	ATCC	CRL-1772
Experimental models: Organisms/strains		
C57BL/6J male mice	Charles River Laboratories	632C57BL/6J
$Bscl2^{lox/lox}$ X Adipoq-CreER mice		Combot et al.[9]
Oligonucleotides		
RPL 19 TCCAGGGCCTTGAGATTGAG GCCAGCGTGCCTTCCA	Sigma-Aldrich	N/A
NGN3 AGTTGGCACTCAGCAAAAAGC GATTGCGCTCCCGATCAT	Sigma-Aldrich	N/A
Neuro D TCCAGGGTTATGAGATCGTCACT CGCTCTCGCTGTATGATTTGG	Sigma-Aldrich	N/A
KI 67 GCGAGCCTCAAGAGATAGCTTCT TTTTGAAGCTTTGGTATCTTGACCTT	Sigma-Aldrich	N/A
INSM 1 TCGCTGTGTTCATGGTCTAGAAA ACGCTACAGACATAGAGAGCAGAGGAT	Sigma-Aldrich	N/A
INS1 TCAGCAAGCAGGTCATTGTTTC AAGCCTGGGTGGGTTTGG	Sigma-Aldrich	N/A
Glucagon GTGACTGGCACGAGATGT AGCACCATTCTGGATAATCTT	Sigma-Aldrich	N/A
Amylase TCCATAAGGATGAGCCAACATAAA GGAGGATCATCCATCCTGACA	Sigma-Aldrich	N/A
ISL1 TGTCATCCCCTGGATATTAGTTTTG GGACAAGAAACGCAGCATCA	Sigma-Aldrich	N/A
PAX4 ACCTGTGCGGTAGTAGCGT AGGGGGACTCTTTGTGAATGG	Sigma-Aldrich	N/A
ARX TCTGTCAGGTCCAGCCTCAT TTCCAGAAGACGCACTACCC	Sigma-Aldrich	N/A
CPA2 GTGCCGTGGAGTCTTTTCAAA CAGATGACTTTAATGAGCTGGATGA	Sigma-Aldrich	N/A
CK19 TCCAGGGCCTTGAGATTGAG GCCAGCGTGCCTTCCA	Sigma-Aldrich	N/A

(*Continued on next page*)

Continued

REAGENT or RESOURCE	SOURCE	IDENTIFIER
Somatostatine CCCAGACTCCGTCAGTTTCTG GGGCATCATTCTCTGTCTGGTT	Sigma-Aldrich	N/A
Snail CAGTGGGAGCAGGAGAATGG TGCACCACCTGTGGAAAGG	Sigma-Aldrich	N/A
NKX 2.2 CGGCGTGAGACGGATGAG AAAGCGCAGACCTACGAGCTG	Sigma-Aldrich	N/A
NKX 6.1 TCCCATCTTTGTCCAACAAAATG GCCCGGAGTGATGCAGAGT	Sigma-Aldrich	N/A
Mafa TCCTCCGGCGTCAGGTT AAAAGCGGTGCTGGAGGAT	Sigma-Aldrich	N/A
PDX1 CCCCAGTTTACAAGCTCGCT CTCGGTTCCATTCGGGAAAGG	Sigma-Aldrich	N/A
18S GATCCGAGGGCCTCACTAAAC AGTCCCTGCCCTTTGTACACA	Sigma-Aldrich	N/A
AREG AAGAAAACGGGACTGTGCAT GGCTTGGCAATGATTCAACT	Sigma-Aldrich	N/A
BMP6 ACTGACTAGCGCGCAGGA TGTGGGGAGAACTCCTTGTC	Sigma-Aldrich	N/A
EREG TTGACGCTGCTTTGTCTAGG GGATCACGGTTGTGCTGAT	Sigma-Aldrich	N/A
MSTN GGCCATGATCTTGCTGTAACC TGTGTGTGTCACCTTGACTTCTAAAA	Sigma-Aldrich	N/A
INHA ACCTGTGAGGACCAGCCA CATAAGTGAAGAGGCCTTCC	Sigma-Aldrich	N/A
VASH2 CCGAGAATCCTTGCCTATCA GCTGCCCATTGGTGAGAT	Sigma-Aldrich	N/A
RH3DML TAACACCTGTAGCAGCATCAATG TAATGGCGTAGTTGCAGACCA	Sigma-Aldrich	N/A
CTRB1 TTCCCTGCTGGGACACTG CAGCTTGTCAGGGGTCTTG	Sigma-Aldrich	N/A
INS2 CATCCACAGGGCCATGTTG CCGCTACAATCAAAAACCATCA	Sigma-Aldrich	N/A
SLC 30a8 TCCGTGCACAGTCTACACATCTG TGGCTGGCAGCTGTAGCA	Sigma-Aldrich	N/A
RFX6 CGGAAGCAGAACAACTCGTTT GTTTGCAAGTTGGAAGCTACTACAGT	Sigma-Aldrich	N/A

(*Continued on next page*)

Continued

REAGENT or RESOURCE	SOURCE	IDENTIFIER
CDKN1A CCTGGTGATGTCCGACCTG CCATGAGCGCATCGCAATC	Sigma-Aldrich	N/A
CDKN1B TTACGTCTGGCGTCGAAGGC AGGCGGTGCCTTTAATTGGG	Sigma-Aldrich	N/A
ABCC8 GGATGGGATGTGCTGGTCAA CAGCCTGCTCAATCGCATCA	Sigma-Aldrich	N/A
GCK CTCGGGTGCAGCTTGTACACGGAGC CGACTCTGGGGACCGAAGGCAGATC	Sigma-Aldrich	N/A
KCNJ11 TTGCCTTTCTTGGACACGAA AAGGGCATTATCCCTGAGGAA	Sigma-Aldrich	N/A
GLP1R CTGGTGCAGTGCAAGTGTCT CTTTCTTTCTCCGCCTTGG	Sigma-Aldrich	N/A
Software and algorithms		
Bioanalyzer 2100 system	Agilent Technologies, CA, USA	N/A
NOVAseq 6000 plateform	Novogene Co., LTD Beijing, China	N/A
FastQC v0.11.9.		N/A
HISAT2 v2.0.5		(56)
HTSeq v0.6.1		(57)
DEseq2 v1.24.0		(58)
Arivis Vision 4D	Zeiss AG	N/A
MATLAB	The MathWorks	R2021a
MeshLab v2022.2		(59)
ImageJ2 V2.9.0		N/A
Leica Qwin500	microsoft	N/A
Cell sens dimension V1.14	olympus	N/A
Other		
mini osmotic pumps	ALZET®	N/A
Glucometer	Accu-checkPerforma, Roche	N/A
binocular microscope	Leica Microsystems, Wetzlar, Germany	N/A
Olympus IX83	Olympus	N/A
QuantStudio 1	Applied Biosystems	N/A
UltraMicroscope II Light Sheet microscope	LaVision BioTec	N/A

EXPERIMENTAL MODEL AND STUDY PARTICIPANT DETAILS

Animals

All procedures involving experimental animals were performed in accordance with the principles and guidelines established by INSERM and were approved by the local animal care and use committee (Charles Darwin ethic committee, Paris, France). Of note, this study included mice at young (8 weeks) or older (52 weeks) age timepoints. However, only male mice were used in the study and this should be considered as a limitation to the generalization of the present research.

C57BL/6J male mice were obtained from Charles River Laboratories (Saint-Germain-sur-l'Arbresle, France) at the age of 8 weeks or 52 weeks. Mice were chow fed *ad libitum* and housed in 12-h light/dark cycles. Mice were acclimatized for 2 weeks in Saint-Antoine research center animal facility (PHEA) before initiating the treatment. Animals were treated with either CORT dissolved in ethanol (25, 50 or 100 μg/mL, as indicated) (Sigma-Aldrich, St. Louis, MO) or vehicle (VEH) (1% ethanol) in drinking water for 3 (aged mice) to 4 weeks (young mice). CORT- and VEH- treatment were changed simultaneously every 2 days. Additionally, treatments were randomly assigned to entire cages. VEH- and CORT-treated mice were located in the same area of the experimentation

room. All experiments with young and old CORT-treated mice were done at the PHEA, institutional permission: C75-12-01, project permission: APAFIS #9533.

For experiments with S961, ALZET mini osmotic pumps were implanted subcutaneously in eight-week-old male C57Bl/6J mice to infuse either S961, an insulin receptor (IR) peptide antagonist (Novo Nordisk) (20 nmol/week), or PBS, as VEH control, at 0.5 μL/h for 1 week as previously described.[15] All experiments with S961 were done at the Institut Cochin animal facility, institutional permission: C75-14-02, project permission: APAFIS # 14856 N° 2018041615405803.

Bscl2$^{lox/lox}$ mice were crossed with Adipoq-CreER[9] mice to generate Bscl2$^{lox/lox}$ X Adipoq-CreER mice as previously described.[10] Cre activation was performed by 5 consecutive days of intraperitoneal Tamoxifen (Tam) injection resuspended in sunflower oil: ethanol (9:1) at 8 weeks-old, and then one injection every month until 6 months. Bscl2$^{lox/lox}$ X Adipoq-CreER mice that receive Tam will be referred as Adipo Seipin KO and Bscl2$^{lox/lox}$ mice treated with Tam will be referred as Adipo Seipin$^{lox/lox}$. Insulin tolerance tests were performed after 6h fasting as previously described (18). All mice (males, n = 8 to 11 per group) were euthanized in the random fed state between 8 a.m. and 10 a.m. All experiments were done in the animal facility, institutional permission D44-278, project permission APAFIS#10980–2017082117591518.

Mouse pancreatic buds were isolated from C57BL/6J female mice (Charles River Laboratories, Saint-Germain-sur-l'Arbresle, France) at precise embryonic day E11.5, pancreatic buds were isolated from embryo using manual microdissection under a binocular microscope as previously described.[38] Experiments were done at Saint-Antoine research center animal facility (PHEA), institutional permission: C75-12-01, project permission: Ce5/2017/002.

Cell lines

The immortalized mouse myoblast cell line C2C12 (gracious gift from Eric Hajduch, INSERM U1138) below passage 7 was used for the *in vitro* experiments.

METHOD DETAILS

Insulin tolerance tests (ITT)

Insulin tolerance tests (ITT) were performed as previously described.[3] Briefly, after a 6-h fast, insulin (1 unit/kg of body weight) was injected intraperitoneally. Blood glucose levels were measured before and 15, 30, 60, and 120 min after the injection, using a glucometer (Accu-check Performa, Roche). Slope of early insulin sensitivity were calculated as the difference of blood glucose levels 15 min after insulin and before insulin injection and divided by time (15 min). Slopes were expressed as mg/dl/min.

Hormonal assays

Blood was collected by intracardiac puncture. Serum was collected after 5 min of centrifugation at 2000*g* at 4°C. Insulin levels were measured using mouse insulin immunoassay (Merck, Millipore) according to manufacturer's instructions.

Islet isolation

Mouse islets were isolated after injecting a collagenase solution (1 mg/mL) (Sigma-Aldrich) in the bile duct and handpicked under a binocular microscope (Leica Microsystems, Wetzlar, Germany) as described in.[3]

Immunohistochemistry, immunofluorescence, and morphometry

Pancreas were dissected - heads and tails separately - then fixed in 3.7% formalin solution, embedded in paraffin, and cut into 5-μm sections. 4 sections per slide were collected at regular intervals throughout entire pancreatic head and pancreatic tail, e.g., if 100 slides were obtained over an entire head, we selected slides #20, #40, #60 and #80 for quantification.

Morphometric parameters (beta-cell fraction, islet size, and density) were evaluated after immunohistochemistry using a mouse monoclonal anti-insulin antibody (Sigma-Aldrich, St. Louis, MO) as described previously.[3] Secondary antibodies coupled to horseradish peroxidase or to alkaline phosphastase were obtained from Jackson ImmunoResearch (Westgrove, PA). Enzyme substrates were DAB+ (Dako). Morphometric parameters were determined by analyzing stained sections using a microscope equipped with a motorized stage and coupled to a camera (Leica Qwin 500) and the Leica Qwin software. Analyzed sections are distant of 20 × 4 × 5 = 400 μm, precluding us from counting twice the same islet, even large objects with an estimated radius of about 60 μm. Each section was entirely analyzed and we measured beta-cell area (μm^2), tissue area (μm^2), numbered and sorted islets based on their size.

Beta-cell fraction (%) was calculated as the ratio of the sum of the insulin-positive areas over the sum of the tissue areas for 8 sections per animal. Beta-cell mass (mg) was calculated by multiplying beta-cell fraction by pancreatic mass. A cluster of more than 4 insulin-positive cells (or a diameter of at least 25 μm) was considered as an islet. Mean islet size (μm^2) was calculated as the total insulin-positive area divided by the total number of islets per pancreas. Islet density (n/mm^2) was calculated as the number of islets per mm^2 of pancreatic tissue. Individual beta-cell size was estimated as described in.[3] Islet were sorted into 9 classes according to their size: Class I [4–11 cells], Class II [12–20 cells], Class III [21–32 cells], Class IV [33–48 cells], Class V [49–66 cells], Class VI [67–87 cells], Class VII [88–112 cells], Class VIII [113–148 cells], Class IX [>148 cells].

Pancreas clearing, imaging and 3D image analysis pipeline

Pancreas collection and clearing

Mice were anesthetized using isoflurane and received 10mL of cold PBS and 20mL of cold 4% paraformaldehyde (PFA) through intracardiac infusion. The dissected pancreata were stored in 20mL of 4% PFA at 4°C for a maximum period of one month. Pancreas staining and clearing was achieved following iDisco clearing technique with an adapted timing. Pancreata were incubated three times with PBS +0.2% Gelatin (Sigma ref. 48723-500-F) + 0.5%TRITON 100X (SigmaT8787) (PBSGT) during 1h at 37°C and incubated in PBSGT for 3 days at 37°C under slow agitation to block nonspecific binding and permeabilize the pancreases.

Permeabilized pancreata were incubated in PBSGT with 0.1–0.2% saponin (Sigma ref S4521) (PBSGT-sap) and mouse anti-insulin antibody (1/800; Sigma I2018) during 5 days at 37°C under slow rotation. Pancreata were washed 6 times in PBSGT at 37°C during 1h under slow agitation and incubated in PBSGT-sap with Alexa 750 coupled anti-mouse antibody (1/50; Life Technologies A21037) for at least 3 days at 37°C under slow agitation. Samples were washed 6 times in PBSGT at 37°C during 1h under slow agitation. At this step, they were either stored in PBSGT at 37°C without agitation for 1 day or directly dehydrated, as follows.

For dehydration, pancreata were first washed two times in H_2O MilliQ at room temperature during 1h under slow agitation, and then, incubated at room temperature under slow agitation in methanol solutions (20%, 40%, 60%, 80% methanol diluted in H_2O MilliQ and two times in 100% methanol) during 1h for each bath. Samples were then incubated overnight in 1/3 methanol +2/3 dichloromethane (DCM; Sigma ref. 270997) solution. Complete delipidation was achieved by 2 incubations of 1h each, at slow agitation, in a bath of pure DCM at room temperature. Immediately after delipidation, pancreases were incubated in dibenzyl ether (DBE; SIGMA ref. 33630) to allow refractive index correction.

3D image acquisitions

Acquisitions of whole pancreases were performed in collaboration with an UltraMicroscope II Light Sheet Fluorescence Microscope magnification 0.63×, dipping cap 2X. An image of the pancreas volume was acquired using tissue autofluorescence (470/40nm excitation filter; 525/50 nm emission filter) with a z-step of 10 μm; islets acquisitions were performed with a z-step of 1 μm (710/75nm excitation filter; 785/62nm emission filter), both using horizontal dynamic focusing.

Islet segmentation and data analysis

Pancreatic islets were segmented automatically using a custom analysis pipeline in Arivis Vision 4D (v3.1.1, Zeiss AG). Briefly: The islet channel in the 3D image was first filtered using a 2D median of radius of 3 pixels. Then two different steps of segmentation were performed. First islets were segmented on the median-filtered image using a threshold on intensity. The value of this threshold was adapted for each image, depending on the preservation of the markers and range with intensity from 180 to 1800 arbitrary units. Spurious objects were filtered out by rejecting objects with a 3D sphericity (without holes) below 0.3, and objects smaller than 100 voxels. The resulting 3D binary mask was then smoothed using the plane-wise 'Closing' morphological filter with a radius of 3 pixels. Because this filtering discarded big islets that had a complex shape and hence, a low sphericity, we used an additional segmentation to rescue them. A second identical step of segmentation was performed, on the same filtered image, but with thresholds on intensity about 50% larger than in the first step and a threshold on sphericity of 0.1. The two binary 3D masks were then exported as meshes, and post-processed in MeshLab (v2022.2) (https://www.meshlab.net). In MeshLab, the islet meshes were determined using the Quadratic Edge Collapse Decimation method, reducing the number of vertices from 40 million to about 5 million per image.

The two meshes from the two segmentation steps were then combined using MATLAB (R2021a, The MathWorks) to produce a single mesh file where each islet is represented by one closed mesh. Individual meshes were then used to yield estimate of the volume, intensity etc. The pancreas volume was segmented from the autofluorescence signal, on an image with larger pixel size, using again Arivis Vision4D. The image was first filtered with a 2D median of radius 3 pixels, then segmented with a threshold on intensity above 200. The resulting 3D binary mask was filtered with the 'Closing' morphological plane-wise operation with a radius 5 pixels.

Islet classification was determine based on our previous method[3] by calculating the volume of an individual beta cell (≈1,670 μm^3) to obtain approximative volume of beta-cell clusters/islets as following:

- $\leq$ 11 cells eq. $\leq$ 18370 μm^3
- 12-20 cells eq. 18371–33400 μm^3
- 21-32 cells eq. 33401–53440 μm^3
- 33-48 cells eq. 53441–80160 μm^3
- 49-66 cells eq. 80161–110220 μm^3
- 67-87 cells eq. 110221–145290 μm^3
- 88-112 cells eq. 145291–187040 μm^3
- 113-148 cells eq. 187041–247160 μm^3
- > 149 cells eq. > 247161 μm^3

Reconstructions presented as Figures 3B and 3C and films in Supplemental data (Movie S1-2) were performed on Blender software using meshes post-process as described above.

Cell and tissue culture

C2C12 cells were grown until reaching confluence in a complete Dulbecco's Modified Eagle's Medium (DMEM) medium containing 4.5g/L glucose, 25 mM pyruvate, (ThermoFisher Scientific, Montigny-le-Bretonneux, France), 10% FBS (fetal bovine serum, Dutscher, Issy-les-Moulineaux, France), glutamine and 1% penicillin/streptomycin. Cells were differentiated into myotubes with a differentiation medium containing DMEM containing 4.5g/L glucose, 25mM pyruvate, 2% horse serum, glutamine and 1%-penicillin/streptomycin (Sigma–Aldrich, Saint Quentin Fallavier; France). The level of differentiation was evaluated under the microscope before initiation of the 24h VEH (ethanol) or CORT (100nM) treatment. Before cell collection, conditioned medium was collected, centrifugated at 2500g for 5 min to remove cellular debris, frozen in liquid nitrogen and stored at −80°C.

Mouse pancreatic buds E11.5 were isolated as previously described[38] and cultured on filters at the interface between air and medium with a control (CTL) medium 100% (RPMI medium, 10% FBS, 1% HEPES, glutamine and 1% penicillin/streptomycin, 1% non-essential amino acids) or CTL medium (50%) mixed with C2C12 conditioned medium (50%). Medium was changed 3 times per week. Pancreatic buds were collected after either 3 days or 7 days of culture in presence of CTL or CTL:C2C12 mix culture medium, or 7 days (CTL:C2C12 mix) + 7 days (CTL 100%) for RNA or protein extraction or immunofluorescent analysis.

In order to analyze the impact of the identified myokines on pancreatic beta-cell differentiation, mouse pancreatic buds E11.5 were isolated and cultured in the absence (control condition, CTL) or in presence of BMP6 (20ng/mL), myostatin (MSTN, 100ng/mL), amphiregulin (AREG, 500ng/mL) or epiregulin (EREG, 100ng/mL). After 3 (D3) and 7 (D7) days of culture, 3 pancreatic buds were pooled and lysed before RNA extraction or individually fixed in 3.7% formalin, included in paraffin and sectioned. Alternatively, after 7 days of culture in the absence or in the presence of the indicated myokine, a 7-day washout culture period in control medium was added (D14). At the end of culture period, 3 embryonic pancreases were pooled in order to perform RNA extraction or individually fixed and sectioned. Immunofluorescence for insulin (Sigma-Aldrich) and glucagon (Sigma-Aldrich) as well as DAPI staining were performed on all sections that were then analyzed as previously described.[38]

RNA analysis – RT-qPCR

Total RNA was isolated (RNeasy Mini Plus Kit or RNeasy Micro plus kit for embryonic buds; QIAGEN, Hilden, Germany) and reverse transcribed into cDNA using the SuperScript III reverse transcriptase kit per manufacturer's instructions (Invitrogen, Carlsbad, CA). Gene expression was quantified by real-time PCR using SYBR Green Supermix (Eurogentec, Seraing, Belgium) in a QuantStudio 1 (Applied Biosystems). The mRNA levels of each specific gene product were calculated using the ddCt method and normalized to reference genes *RPL19 or 18S* expression level. Values are expressed as the fold change of the treated compared to the control condition.

RNA analysis – RNAseq

Total RNA was extracted from 3 replicates of C2C12 cells differentiated into myotubes and treated for 24h with either DMSO (VEH) or Corticosterone (CORT) (100nM). RNA was extracted from cells using Qiagen RNeasy mini kit per manufacturer's instructions (Qiagen, Hilden, Germany). RNA integrity (RIN) was assessed using Bioanalyzer 2100 system (Agilent Technologies, CA, USA). RNA with a RIN above 9 were used to establish the sequencing libraries. PolyA mRNA selection, cDNA libraries preparation and sequencing were conducted by Novogene Co., LTD (Beijing, China) using the Illumina NOVAseq 6000 plateform and 150bp paired-end reads sequencing.[39] Sequencing depth ranged from 28′851′292 to 36′073′937 reads per sample. Read quality check was examined using FastQC v0.11.9. Clean reads were obtained using Fastp v0.20.1 to remove low-quality reads and read adapters. Clean reads were mapped on the USCS *Mus musculus* mm10 reference genome using HISAT2 v2.0.5 default parameter.[40] Transcript abundance was quantified using HTSeq v0.6.1 using -m union parameter.[41] The differential expression analysis was performed using the DEseq2 v1.24.0 package.[42] Genes with an adjusted p-value <0.05 were further used for analysis. R software and ggplot2 v3.3.4 were used to generate volcano plots and perform the principal component analysis in-between CORT-vs. DMSO-treated myotubes. Gene ontology, pathways enrichment analysis and protein-protein interaction networks with a Padj< 0.05 were generated using GOSeq v1.34.1, STRING-database,[43] KEGG[44] (KOBAS v3.0) and Wikipathways databases (https://wikipathways.org). RNAseq raw data are deposited on the NCBI Gene Expression Omnibus (GEO) repository under the accession number GSE261984, BioProject: PRJNA1089982.

Western Blot

Cells and pancreatic buds were extracted as previously described.[3] Protein lysates were separated by SDS-PAGE, transferred onto nitrocellulose membrane (Thermofisher, scientific) and immunodetected with antibodies targeting either total AKT (Rabbit polyclonal anti-AKT, Cell Signaling Technology), phosphor AKT (Rabbit polyclonal anti-Phospho-AKT (Ser 473), Cell Signaling Technology), PDX1 (64), Ki67 (Rabbit polyclonal antibody, Abcam, ab15580), PCNA (Rabbit polyclonal antibody FL-261, Santa Cruz), Tubulin (Monoclonal anti a-tubulin, Sigma-Aldrich). Bands were detected with Supersignal West Pico PLUS chemiluminescent substrate (Thermofisher scientific, per manufacturer's instructions) and imaged on a camera iBright CL1500 (Thermofisher scientific). Bands intensities were quantified using the open-source ImageJ software.

Kinome profiling

Pancreatic islets and ducts from either 4 weeks CORT- or VEH-treated young mice were isolated after injecting a collagenase solution (1 mg/mL, Sigma-Aldrich) in the bile duct and handpicked under a binocular microscope (Leica Microsystems, Wetzlar,

Germany) as described in.[3] For kinome analysis, sample incubation, detection and analysis were performed on a PamStation 12 following the manufacturer's instructions as previously described[45,46] using serine/threonine or tyrosine kinase PamChip microarrays (PamGene International BV). Upstream kinases were identified using the Human Protein Reference Database (http://www.hprd.org/). Functional enrichment analysis and protein-protein interactions were identified on STRING database[43] and by generating a new dataset combining kinases, phosphoproteins and myokine candidates.

QUANTIFICATION AND STATISTICAL ANALYSIS

(1) For all analysis, quantifications and *p* values are indicated in the figure legend.
(2) Insulin tolerance tests (relate to Figures 1, S1, and S2) were performed on C25 (n = 6), C50 (n = 6), C100 (n = 5) or VEH (n = 6) young C57BL/6J male mice (Figure 1); on VEH (n = 4), C25 (n = 4), C50 (n = 4) and C100 (n = 4) older C57BL/6J male mice (Figure S1); or on Seipin KO mice (n = 9) vs. WT mice (n = 10) (on VEH (n = 4), C25 (n = 4), C50 (n = 4) and C100 (n = 4) older C57BL/6J male mice (Figure S2). Values are expressed as the mean ± SEM. Statistical analysis was done using the GraphPad Prism 9 software and a one-way ANOVA multiple comparison test or Mann-Whitney *U* test (Figure 1B – slope of insulin sensitivity). $P < 0.05$ was considered significant.
(3) Pancreas 2D morphometric analysis (related to Figures 1, S1, and S2) was done on VEH (n = 4), C25 (n = 5), C50 (n = 4) and C100 (n = 5) young C57BL/6J male mice (Figure 1); or VEH (n = 5), C25 (n = 6), C50 (n = 4) and C100 (n = 4) older C57BL/6J male mice (Figure S1); or on Adipo Seipin KO (n = 7) or L/L (n = 7) mice (Figure S2); or S961-treated (n = 6) or VEH (n = 4) mice (Figure S2). Per pancreas, quantification was performed to determine islet volume, islet density, mean islet size and beta-cell mass. Alternatively, Adipo Seipin KO (n = 3) or L/L (n = 4) mice, S961-treated (n = 4) or VEH (n = 4) were used for alpha-cell fraction and mass calculation (Figures S2I, S2J, S2Q, and S2R). Values are expressed as the mean ± SEM. Statistical analysis was done using the GraphPad Prism 9 software and Mann-Whitney *U* test (Figure S2) or one-way ANOVA multiple comparison (Figures 1 and S1). $P < 0.05$ was considered significant.
(4) 3D pancreas analysis was performed on VEH- (n = 4) and C50-treated (n = 5) young C57BL/6J male mice (Figure 2); or VEH (n = 3) and C50-treated (n = 4) older C57BL/6J male mice (Figure S3). Please see the method section named ''islet segmentation and data analysis'' for more details. For C50 vs. VEH morphometric analysis and islet clusters analysis, values are expressed as the mean ± SEM. Statistical analysis was done using the GraphPad Prism 9 software and Mann-Whitney *U* test vs. VEH (Figure 2 and S3). $P < 0.05$ was considered significant.
(5) For *in vitro* analysis of C2C12 differentiated myotubes and pancreatic buds treated with conditioned medium (Figure 3), VEH (n = 6) or C50 (n = 6) biological replicates were done to estimate insulin resistance (Figure 3A); CM VEH (n = 4), CM CORT (n = 3) pancreatic buds were used to analyze beta-cell fraction, (no CM (n = 2) is given as an indication); pancreatic buds RT-qPCR analysis were performed on CM VEH (n = 4) or CM C50 (n = 4) at either D7 or D14 using the ddCt method and normalized to the reference gene *18S* expression level. values are expressed as the mean ± SEM. Statistical analysis was done using the GraphPad Prism 9 software and two-way ANOVA test (Figure 3D). $P < 0.05$ was considered significant.
(6) 3 independent biological replicates of C2C12 cells differentiated into myotubes and treated for 24h with either DMSO (VEH) or Corticosterone (CORT) (100nM) were used for RNAsequencing analysis as described in the Method or in the Result sections related to Figure 3. 29 to 35 million reads, paired-end 150bp long, were generated using the Novaseq 6000 illumina sequencer. The analysis pipeline included: quality check, read filtering, alignment on the mm10 genome, count normalization and statistical analysis using FastQC v0.11.9., Fastp v0.20.1, HISAT2 v2.0.5, HTSeq v0.6.1, DEseq2 v1.24.0. QC stats and principal component analysis are reported in Figure S4. Differentially expressed genes with an adjusted p-value (false discovery rate) < 0.1 and a log2fold change of ±0.5 were further used for analysis and reported in Table S2).
(7) Gene expression analysis (Figures 3G, 3H, 4D–4K, S4, and S6) was calculated using the ddCt method and normalized to the reference gene *18S* expression level. Figure 3G VEH: n = 9, C50: n = 10 for *MSTN*; VEH: n = 3, C50: n = 6 for *AREG*; VEH: n = 7, C50: n = 8 for *EREG*; VEH: n = 6, C50: n = 6 for *BMP6*; Figure 3H VEH: n = 20, C50: n = 21 for *MSTN*; VEH: n = 11, C50: n = 10 for *AREG*; VEH: n = 16, C50: n = 14 for *EREG*; VEH: n = 20, C50: n = 21 for *BMP6.* Figure S4 n = 4 per condition except for MSTN (n = 2). Of note, a minimal amount of 3 pancreatic buds were combined per condition before RNA extraction (Figure 3 and S6). Figures 3G, 3H, and S4: Statistical analysis was done using the GraphPad software and a Mann-Whitney test. Figures 4 and S6: statistical analysis was done using the GraphPad Prism 9 software by testing first normality of the sample (Shapiro-Wilk test) and second using two-way ANOVA multiple comparison. $P < 0.05$ was considered significant.
(8) Kinome assay (Figure S5) performed on pancreatic ducts and pancreatic islets protein extracts of CORT- or VEH-treated mice (n = 4 mice per group). Data analysis was done with Bionavigator software from Pamgene. Statistical analysis was done using a Student *t*-test.